Developing snowflake divertor physics basis in the DIII-D, NSTX and NSTX-U tokamaks aimed at the divertor power exhaust solution.

V.A. Soukhanovskii[a], S.L. Allen[a], M.E. Fenstermacher[a], C.J. Lasnier[a], M.A. Makowski[a], A.G. McLean[a], E.T. Meier[a,1], W.H. Meyer[a], T.D. Rognlien[a], D.D. Ryutov[a], F. Scotti[a], E. Kolemen[b], R.E. Bell[b], A. Diallo[b], S. Gerhardt[b], R. Kaita[b], S. Kaye[b], B.P. LeBlanc[b], R. Maingi[b], J.E. Menard[b], M. Podesta[b], A.L. Roquemore[b], R.J. Groebner[c], A.W. Hyatt[c], A.W. Leonard[c], T.H. Osborne[c], T.W. Petrie[c], J.-W. Ahn[d], R. Raman[e], J.G. Watkins[f]

[a]Lawrence Livermore National Laboratory, 7000 East Ave, Livermore, CA 94550, USA

[b]Princeton Plasma Physics Laboratory, PO Box 451, Princeton, NJ 08543-0451, USA

[c]General Atomics, PO Box 85608, San Diego, CA 92186-5608, USA

[d]Oak Ridge National Laboratory, Oak Ridge, TN 37831, USA

[e]University of Washington, Seattle, WA 98195, USA

[f]Sandia National Laboratories, PO Box 969 Livermore, California 94551-0969, USA

Abstract*— Experimental results from the National Spherical Torus Experiment (NSTX), a medium-size spherical tokamak with a compact divertor, and DIII-D, a large conventional aspect ratio tokamak, demonstrate that the snowflake (SF) divertor configuration (D.D. Ryutov, Phys. Plasmas, 14, 064502, 2007) may provide a promising solution for mitigating divertor heat loads and target plate erosion compatible with core H-mode confinement in future fusion devices, where the standard radiative divertor solution may be inadequate. In NSTX, where the initial high-power SF experiment were performed, the SF divertor was compatible with H-mode confinement, and led to the destabilization of large ELMs. However, a stable partial detachment of the outer strike point was also achieved where inter-ELM peak heat flux was reduced by factors 3-5, and peak ELM heat flux was reduced by up to 80 % (cf. standard divertor). The DIII-D studies show the SF divertor enables significant power spreading in attached and radiative divertor conditions. Results include: compatibility with the core and pedestal, peak inter-ELM divertor heat flux reduction due to geometry at lower n_e, and ELM energy and divertor peak heat flux reduction, especially prominent in radiative D_2-seeded SF divertor, and nearly complete power detachment and broader radiated power distribution in the radiative D_2-seeded SF divertor at $P_{SOL} = 3 - 4$ MW. A variety of SF configurations can be supported by the divertor coil set in NSTX Upgrade. Edge transport modeling with the multi-fluid edge transport code UEDGE shows that the radiative SF divertor can successfully reduce peak divertor heat flux for the projected $P_{SOL} \simeq 9$ MW case. The radiative SF divertor with carbon impurity provides a wider n_e operating window, 50% less argon is needed in the impurity-seeded SF configuration to achieve similar q_{peak} reduction factors (cf. standard divertor).

I. Introduction

An axisymmetric poloidal magnetic X-point divertor is the present vision for the tokamak plasma-material interface. The divertor enables access to high core and pedestal plasma performance metrics while keeping target plate heat loads and erosion within the operating limits of plasma-facing component cooling technology and target materials. The proposed ITER divertor is based on standard X-point geometry designs tested in large tokamak experiments: vertical targets with partial radiative detachment of the strike points are used. However, the standard radiative divertor approach is likely to be insufficient for next step advanced tokamak and spherical tokamak devices such as the proposed fusion nuclear science facilities or the DEMO reactor. Magnetic divertor configuration development and optimization has been an active area of fusion research since the 1070's [1]. Many advanced divertor concepts (w.r.t. the standard divertor) rely on modifications to parallel and perpendicular transport, dissipative loss channels, and increased plasma-wetted area via modification of the magnetic configuration.

A snowflake divertor (SF) configuration [2] is a promising tokamak power exhaust concept that has received experimental support from TCV [3], NSTX [4], DIII-D [5] and EAST tokamaks [6]. The SF magnetic configuration uses a second-order null-point created by superimposing two first-order poloidal field nulls, leading to the snowflake-like separatrix branches in the region of the exact second-order null, and a broader low B_p region, due to a quadratic B_p dependence on the distance (vs linear B_p dependence in the standard divertor). These magnetic properties have a strong impact on divertor transport and heat deposition on plasma-facing components, owing to the increased divertor plasma-wetted area, increased X-point-to-target connection length and divertor volume, and additional divertor legs (strike points) where heat and particles can flow [2], [7], [8]. In this paper we summarize high divertor power-density experiments in the NSTX and DIII-D tokamaks, and discuss the results in the context of the SF concept development for future devices.

II. Magnetic equilibria and control

Snowflake divertor configurations have been developed and demonstrated on a medium-size spherical tokamak NSTX and a large conventional aspect ratio tokamak DIII-D. Both

[1]Presently at College of William and Mary, Williamsburg, VA, USA

978-1-4799-8264-6/15/$31.00 ©2015 IEEE

	Minor radius a (m)	P_{NBI} (MW)	I_p (MA)	λ_q (mm)	f_{exp} Standard / SF	$L_{\|\|}$ Standard / SF	D (m)
NSTX	0.58	4	0.9	5-6	10-20 / 30-80	10-12 / 15-60	0.125
DIII-D	0.60	5	1.2	2.5-3	10 / 30-40	50 / 50-150	0.1
NSTX-U	0.62	≤ 12	≤ 2	~ 3	10-20 / 40	7-15 / 20-30	0.11

TABLE I

PLASMA AND ENGINEERING PARAMETERS IN THE NSTX AND DIII-D SNOWFLAKE DIVERTOR EXPERIMENTS, AND THE PLANNED ONES FOR NSTX-U.

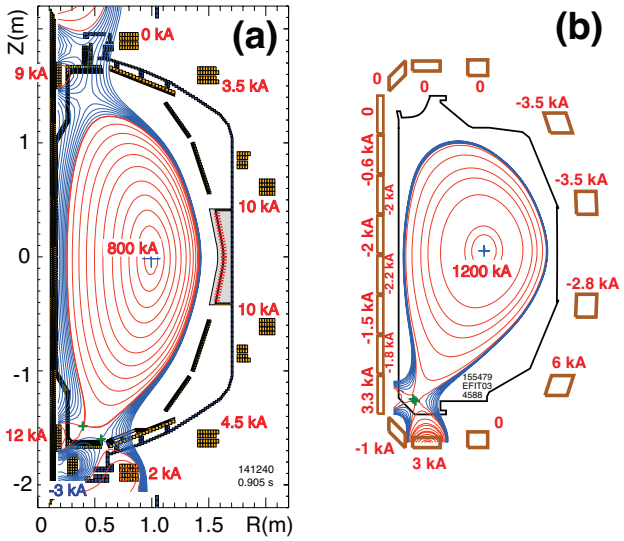

Fig. 1. Experimental equilibria with the SF divertor configuration obtained in (a) NSTX and (b) DIII-D tokamaks. Poloidal field coil currents are indicated.

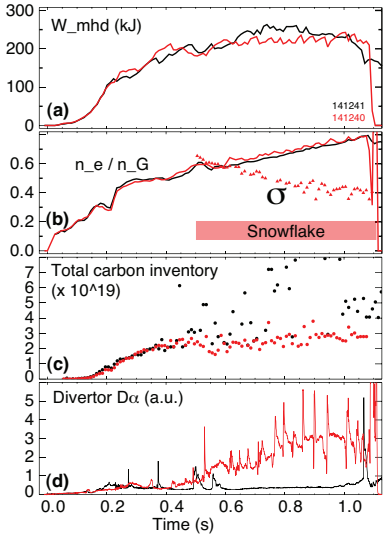

Fig. 2. Time traces of the H-mode discharges with the standard divertor (black) and SF (red): (a) Plasma stored energy W_{MHD}; (b) n_e/n_G and σ; (c) total carbon inventory N_C; (d) lower divertor D_α intensity.

tokamaks have open divertors with graphite plasma-facing components and divertor heat fluxes of several MW/m^2. Both tokamaks have a similar poloidal field coil layout. Three magnetic coils available for the snowflake configuration in the divertor region (Fig.1). The exact second-order null configuration is topologically unstable [2], therefore, in experiments, the following variants are realized in steady-state [9], [10]: (1) the snowflake-plus (SF-plus), where the secondary null is at a small finite distance on the private flux region side of the standard divertor X-point; (2) the snowflake-minus (SF-minus), where the secondary null is in the common flux scrape-off layer (SOL) region; (3) the near exact SF, where the distance between the nulls is approaching zero, while the configuration is fluctuating between SF-plus, SF-minus, and exact SF. The plasma control systems in both tokamaks are similar. Pre-programmed coil currents and strike point position control by the plasma control system (as in Ref. [11]) were used for SF-minus configurations. A real-time null-tracking algorithm was used for control of the near exact SF and SF-plus [12]. The SF configurations were sustained for periods comparable with plasma discharge duration, exceeding many energy confinement times: up to 0.5 s in NSTX, and for 2-3 s in DIII-D.

Under certain conditions, the derivative SF configurations, the SF-plus and SF-minus, have similar properties to those of the exact second order null SF configuration. Two criteria have been developed theoretically for the separation of the poloidal field nulls to describe the situations when the SF-plus and the SF-minus are similar to the exact SF in (1) geometry properties, and (2) enhanced transport, leading to the power sharing between four strike points [7]. The SF-plus and SF-minus geometry parameters, e.g., the poloidal magnetic flux expansion, the magnetic connection length, the divertor specific volume are increased w.r.t. the standard divertor similarly to the exact SF configuration when the distance D between nulls satisfies $D \leq a\ (\lambda_q/a)^{1/3}$ (where a is the minor radius and λ_q is the SOL power width (projected to midplane)). The criterion for the enhanced transport in the SF-plus and SF-minus is $D \leq D^* \sim a\ (a\beta_{pm}/R)^{1/3}$, where D^* is the radius of the high-convection zone in the null-region, expressed as a function of a, R and the midplane poloidal β. The appropriate parameters realized in the NSTX and DIII-D experiments are summarized in Table II. The inter-null distance D obtained in the experiments is within 50 % of the estimated. It is noted that the geometry and transport properties in the SF-plus and the SF-minus may be affected even when the inter-null distances are larger than those from the criteria. The criteria provide guiding estimates as to when the second null affects the geometric and transport properties most significantly.

III. SNOWFLAKE DIVERTOR EXPERIMENTS IN NSTX.

The SF divertor experiments were performed using highly-shaped, lower single null biased ($drsep \simeq 6-7$ mm) $I_p = 0.8$ MA H-mode discharges with 4 MW NBI heating at $B_t = 0.45$ T and the ion ∇B direction toward the lower divertor.

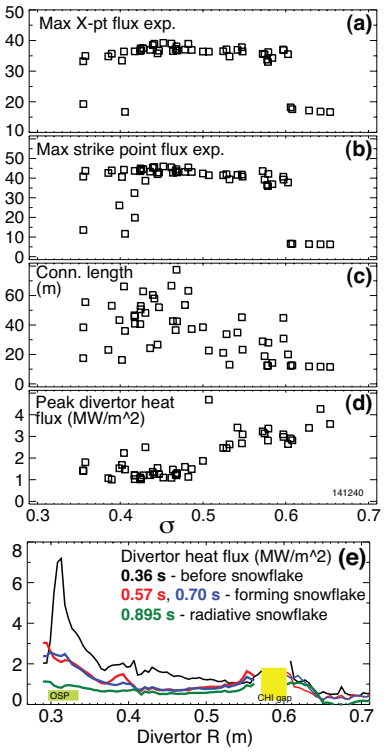

Fig. 3. Divertor geometry parameters and between-ELM peak heat flux as functions of σ: maximum f_{exp} in the (a) X-point and (b) outer strike point regions; (c) connection length $L_{\|}$; (d) peak heat flux. (e) Divertor heat flux profiles before, during, and after SF-minus formation).

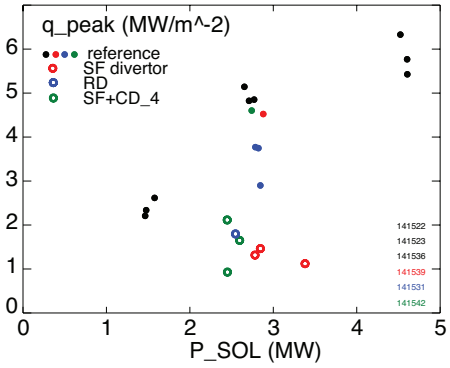

Fig. 4. Peak divertor heat flux q_{peak} as a function of scrape-off layer power P_{SOL} for the standard divertor discharges (filled circles) and the RD and SF discharges (open circles).

The SOL power (estimated from the core power balance) was $P_{SOL} \simeq 3$ MW. Lithium coatings were used for wall conditioning and fuel inventory control in the amount of 80-100 mg per discharge. The core plasmas with SF configurations had similar shaping parameters w.r.t. to those achieved with the standard divertor: the plasma volume ($V \simeq 12$ m^3) and elongation ($\kappa \simeq 2.2 - 2.4$) were unchanged, whereas the bottom triangularity was slightly reduced ($\delta \sim 0.65 - 0.8$).

The SF configuration was compatible with high confinement plasma operation, with no degradation in H-mode core performance [4], [11]. Shown in Fig. 2 are the time traces of two discharges with the standard and the SF configurations. The SF configuration was realized at $n_e/n_G \simeq 0.6 - 0.8$. Core plasma parameters ($\bar{n}_e$, central $T_e \leq 1$ keV, $\beta_N \leq 4.5$) were similar in the two discharges. Similar high performance metrics of these discharges, e.g., $\tau_E \simeq 50 - 60$ ms, $W_{MHD} \simeq 200 - 250$ kJ, and the confinement factor H98(y,2) $\simeq 1$, confirmed minimal, if any, impact of the SF phase on confinement. In these high-triangularity plasmas, the L-H transition power threshold was fairly low (about 1 MW), therefore no H-mode threshold studies were performed. The transition to the SF configuration in NSTX led to a clear and reproducible destabilization of ELMs. As the normalized inter-null distance $\sigma = d_{xx}/a$ became less than 0.5, large ELMs were evident on the lower divertor D_α time traces (Fig. 2 (b), (d)). These large ELMs were classified as Type I, with somewhat irregular frequency of $f = 12 - 35$ Hz and $\Delta W_{MHD}/W_{MHD} \leq 15$ %. In the standard divertor H-mode discharge, lithium coatings on lower divertor PFCs reduced recycling and led to modified edge plasma pressure and current profiles and low-n peeling-ballooning mode stabilization [13], [14], as the pedestal stability operating point was close to the peeling boundary. Depending on the lithium conditioning and other operational factors, ELMs were completely or partially suppressed in standard divertor H-mode discharges. Understanding of the SF pedestal stability in NSTX is complicated by this and other factors, e.g., the uncertainties in the electron pressure gradient and edge toroidal current density, plasma shaping changes (e.g. bottom triangularity), and the radiative detachment that accompanied the SF transition. In general, in the SF phase, the pedestal T_e was slightly reduced, while the pedestal n_e was also reduced due to reduced carbon density. The SF divertor phase had a strong effect on plasma impurity content (Fig. 2 (c)): the total carbon inventory N_c was reduced by 50-70 %. The observed reduction was attributed to the particle expulsion effect from the ELMs that appeared in the SF phase [11].

The SF-minus geometry had a strong impact on divertor properties in NSTX. The SF-minus formation always led to a stable partial detachment of the outer strike point, otherwise inaccessible in the standard divertor at $P_{SOL} = 3$ MW at $n_e/n_G = 0.6 - 0.8$ [15], [16]. A significant inter-ELM reduction of divertor peak heat flux was measured [4], [11].The heat flux reduction was interpreted as driven by both the geometric changes ($L_{\|}$, A_w) and the increased radiative and momentum losses. Shown in Fig. 3 are divertor geometry factors and peak heat flux between ELMs as functions of the σ parameter. Fairly clear trends can be seen albeit some data scatter. Note that the σ parameter was large ($\sigma \geq 0.6$, if meaningful) for the standard divertor, and the data for $\sigma \geq 0.65$ is not plotted. During the transition from the standard to SF geometry ($\sigma = 0.55 - 0.65$), divertor q_{peak} decreased concomitantly with increasing f_{exp} and $L_{\|}$. At $\sigma \leq 0.55$, a partial strike point detachment was observed, apparently driven by further increases in the SOL collisionality and volumetric losses from increased $L_{\|}$ and divertor volume. Fig. 3 (e) shows the divertor heat flux profiles at various times. During the SF formation period that lasted for 100-200 ms, divertor power decreased from 1.8-2.0 MW to about 1.2 MW, and the peak heat flux was reduced from 4-7 MW/m^2 to 2-3 MW/m^2 between ELMs. After the onset of detachment ($t \simeq 0.700$ s), q_{peak} further decreased to 0.5-1 MW/m^2, while the total

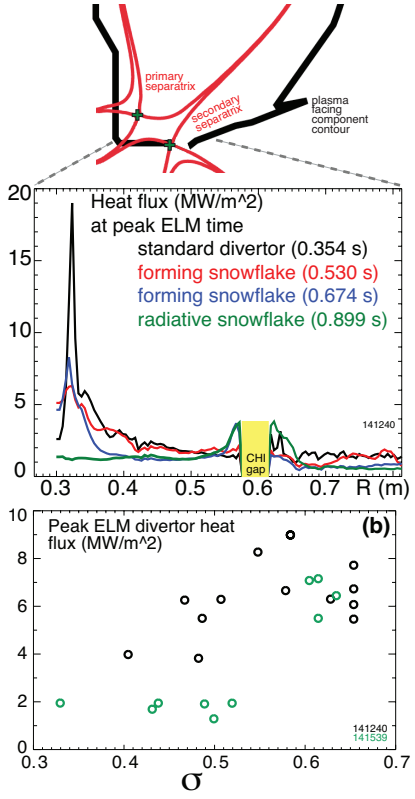

Fig. 5. (a) Peak divertor heat flux at peak ELM times before and during the SF formation, as well as in the radiative SF phase. The upper inset shows two separatrix branches in the asymmetric SF-minus configuration. (b) Peak divertor heat fluxes measured at peak ELM times as functions of the σ parameter.

power received by the outer divertor decreased to below 1 MW. A detailed comparison of divertor impurity radiation and recombination profiles in the SF-minus was presented elsewhere [11]. In spite of the formation of the highly-radiating detached region in the SF divertor, high core confinement was maintained.

The peak heat flux reduction in the SF configuration (without D_2 seeding) was similar to that measured in the the radiative divertor experiments in the standard divertor geometry with D_2 or CD_4 seeding at similar $P_{SOL} \sim 3$ MW. These results are summarized in Fig. 4. Experiments were also performed with additional CD_4 or D_2 seeding into the SF phase using a divertor gas injector. In the CD_4-seeded SF divertor, the divertor C III and C IV brightness profiles showed (cf. standard radiative divertor) increased radiation, both in the intensity,and in the spatial extent. Excellent divertor gas screening from the core, increased divertor radiation, and stable MARFE-free operation (unaffected confinement) were demosntrated [17].

The SF-minus configuration had a strong impact on ELM heat fluxes in NSTX (Fig. 5). Peak heat fluxes from Type I ELMs were significantly reduced, from about 5-20 MW/m^2 in the standard divertor phase of the discharge, to 6-8 MW/m^2 during the SF formation phase and eventually below 2 MW/m^2 in the radiative SF phase. Peak target temperatures, measured by infrared thermography at peak ELM times, reached 1000-1200 ^{o}C in the standard divertor and only 300-500 ^{o}C in the

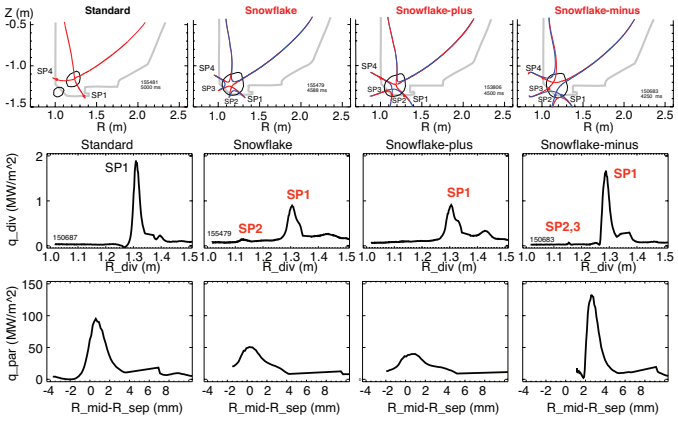

Fig. 6. Experimental equilibria of the standard, SF, SF-plus, and SF-minus divertor configurations. The primary separatrices are shown by the red lines, the secondary by the blue lines. The region $B_p \leq 0.1\ B_{pm}$, where B_{pm} is the outer midplane B_p, is shown by the line surrounding the null(s) region. Inter-ELM divertor deposited and parallel heat flux profiles in the standard ($D \simeq 20$ cm), SF ($D \leq 3$ cm), SF-plus ($D \leq 10$ cm), and SF-minus ($D \leq 11$ cm) configurations.

SF phase. Peak ELM heat fluxes showed a decreasing trend with decreasing σ, while the the plasma stored energy loss due to ELMs ΔW_{MHD} either decreased or remained similar during the transition from the standard divertor to the SF-minus (decreasing σ). The surface temperature rise is given by $\Delta T \sim E_{ELM}/(A_w \times \sqrt{\tau_{ELM}})$. Reduced surface heating was expected due to the increased ELM energy deposition time τ_{ELM} and increased A_w as the ELM convective ion heat pulse with energy E_{ELM} travels over an increased field line length $L_{||}$ connecting the outer mid-plane to the divertor target, as also confirmed by modeling [18]. Another possible effect is the theoretically predicted convective mixing of the ELM heat in the null-point region leading to the heat flux partitioning between separatrix branches, and driven by the loss of MHD equilibrium, balooning modes and flute-like instabilities in the null-region [8]. The emergence of an additional peak in the heat flux (and temperature) profile at the secondary separatrix location (and also where f_{exp} and L_X were close to those of the standard divertor) and a strong reduction of heat flux at the primary separatrix was consistent with the theoretically predicted SF power sharing effects, and a strong baffling of ELM heat flux in the detached SF-minus. The heat flux in the inner divertor, that usually receives more heat during ELMs in tokamaks [19]–[21], was not measured in these experiments.

IV. Snowflake divertor experiments in DIII-D.

The SF divertor experiments were conducted in DIII-D using a standard highly-shaped lower single null H-mode discharge scenario with $B_t = 2$ T, $I_p = 1.2$ MA, $P_{NBI} \leq 5$ MW, and ion $B \times \nabla B$ drift toward the lower divertor. A divertor cryo-pump was used for particle removal, and D_2 seeding was used for steady-state density control in the range $(0.4 - 0.7) \times n_e/n_G$ ($\sim 4.5 - 7.5 \times 10^{19}$ m^{-3}, where n_G is the Greenwald density [22]).

Inter-ELM peak heat flux reduction in the SF divertor (cf. standard divertor) were observed in the experiments and attributed mostly to the increased A_{wet} and $L_{||}$. Shown in

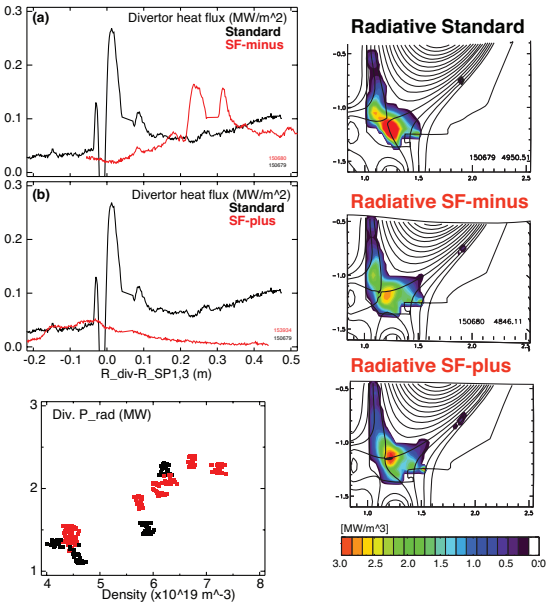

Fig. 7. Inter-ELM divertor heat flux profiles in the standard radiative, SF-minus (a), and SF-plus (b) divertors. Divertor radiated power as a function of core plasma density. Radiated power distribution on the standard radiative, SF-minus and SF-plus configurations.

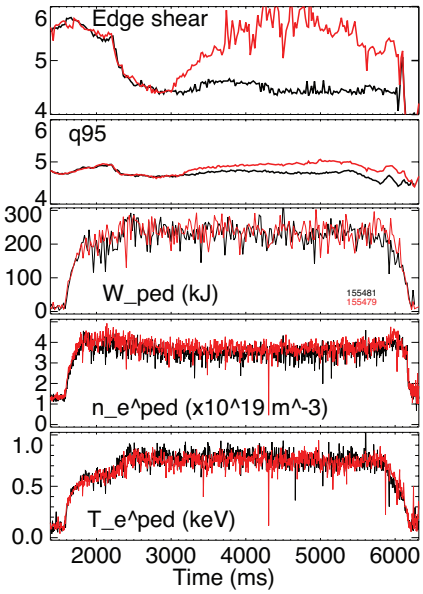

Fig. 8. Edge and pedestal time traces with the standard (black) and SF (red) configurations. (a) Edge magnetic shear; (b) q95; (c) Pedestal energy; (d) Pedestal density; (e) Pedestal temperature.

Fig. 6 are the divertor heat flux profiles measured in 4-5 MW NBI-heated H-modes by infrared thermography under attached divertor conditions (lower $n_e \sim (4-5.5)\times 10^{19}$ m^{-3}) with similar low divertor radiated power losses (1.3 MW). Also shown are the parallel heat flux profiles, where the effect of A_{wet} is accounted via the angle between the total magnetic field and the divertor target: $q_{||} = q_{div}/\sin(\alpha)$, where $\alpha = 0.5-2°$. The inter-ELM profiles were conditionally averaged over 20-50 ms during the last 25% of the inter-ELM cycle. In all SF divertor configurations, the innermost SP (SP4 referring to Fig. 6) received low heat flux 0.1-0.3 MW/m^2, similar to the standard divertor. Power spreading in the divertor via heat flow into additional divertor legs (SP2, SP3) was also observed. In the SF-minus, outer SOL power was split between SP3 and SP1. The fraction of power (and heat flux) deposited in SP3 was typically low, up to 15 % of the power measured in the SP1 at $P_{NBI} \geq 5$ MW, and undetectable at $P_{NBI} \leq 4$ MW, despite the fact that 30-60% of the SOL adjacent to the primary separatrix was connected to it. Interestingly, the SP1 received most of the heat flux, which was mitigated due to the increased flux expansion [23]. In the nearly-exact SF, most of the outer SOL heat went into the SP1, and a small fraction (again, up to $\sim$ 10%) diffused across the null region into SP2. Heat deposition in the SF-plus was similar, except heat in the additional SPs was rarely detected, likely to be because of the proximity of the 45-degree divertor tile to the secondary null and the associated high flux expansion. In most cases, the A_{wet} accounted for up to 80-90% of the observed divertor q_{peak} reduction, with the rest attributed to other effects, e.g. spreading to the additional SPs, and not readily quantifiable reduction due to additional diffusive spreading over the increased $L_{||}$ [23], [24].

Radiative SF divertor experiments in DIII-D revealed stronger inter-ELM divertor peak heat flux reduction in comparison with the standard radiative divertor. Radiative divertor conditions in DIII-D are achieved in the standard divertor with carbon and deuterium radiation using D_2 seeding that increases upstream (and core) density [25], [26]. A comparison of the D_2-seeded radiative SF and standard radiative divertor results at $P_{NBI} = 4-5$ MW are shown in Fig.7 and can be summarized as follows. (1) Both the radiative SF-plus and SF-minus were compatible with the H-mode confinement albeit with confinement degradation similar to the standard divertor. While the confinement degradation was not associated with the SF formation at lower-to-medium densities, additional D_2 seeding at rates 50–80 Torr l/s (to raise the density for radiative divertor onset) resulted in 10%-20% reduction in, e.g., H98(y,2) and H89L factors and plasma stored energy W_{MHD} in the standard divertor, and up to 30% in H-mode discharges with the radiative (higher-density) SF-plus or SF-minus. The degradation was associated with the reduction of pedestal T_e^{ped} and hence pedestal energy [23]. Further H-mode scenario development is necessary to optimize compatibility of the core plasma with radiative SF, as is typically done with the standard radiative divertor (e.g., Ref. [27]). (2) Divertor heat flux profiles are compared in Fig. 7 (a,b). In the standard divertor, the partial detachment led to a significant (up to x10) peak heat flux reduction (cf. Fig. 6). In the radiative SF-minus and SF-plus, a nearly complete power detachment was observed, as heat flux in SP1 was barely detectable. The flux expansion factor could account for most of the difference between the radiative SF-minus and the standard divertor, while in the SF-plus case, the difference was greater. (3) The onset of radiative SF conditions (e.g., increase in impurity radiation and recombination, heat flux reduction) were obtained at core n_e similar (or lower by 10-20%) to the standard radiative divertor. The radiated power was more broadly distributed in the SF configurations, including

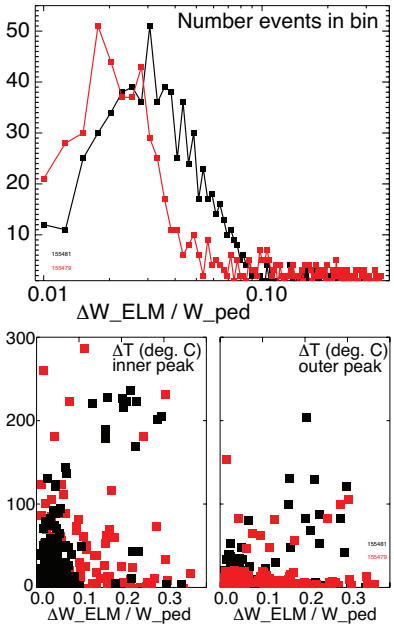

Fig. 9. Distribution of ELM energy normalized to pedestal energy in the standard and SF configurations. Peak divertor temperatures due to ELMs in the inner and outer strike points in the standard and SF configurations.

the additional divertor legs. Shown in Fig. 7 are radiated power distributions in the radiative standard and SF divertors, obtained from tomographic reconstructions of multi-channel bolometry data. The lower divertor radiated power was about 2 MW in the radiative standard, SF-plus or minus configurations, differing by 10%-15% (cf. $P_{SOL} \sim 3.0 - 3.5$ MW). In the standard divertor, radiation initially peaked in the inner and outer divertor legs, and at the partial detachment onset, the radiative front moved to the X-point (e.g., Ref. [26]). In the SF-minus, radiation also initially peaked in the divertor legs, and, as the SF-minus was formed, it broadly distributed throughout the divertor volume, with occasional peaking at the null-points. In the SF-plus, the radiation front was formed in the divertor legs and moved toward the null-point region where it stabilized. The extended connection length region enabled a broader radiation zone. Despite the geometric effects (e.g., increase in $L_{||}$ by 50%-75%), the SF configurations were not more likely than the standard divertor to form X-point radiative instabilities that could degrade the confinement.

Initial experiments were also performed to combine the radiative SF divertor configuration with a high-performance advanced tokamak H-mode scenario [28]. The configuration included the upper single null and lower snowflake-minus with the ion ∇B direction toward the upper divertor, and neon and D_2 seeding. While the peak heat flux reduction was about 50 % stronger in the radiative SF than in the standard radiative divertor with comparable core confinement (e.g., H98(y,2) $\sim$ 1.30, $\beta_N \sim$ 2.9), neon accumulation was 3040 % higher in the radiative SF case. As cryopumping was used for neon inventory control, the need for better understanding of compatibility of cryopumping with high flux expansion was concluded.

Returning to the core and pedestal with the SF configuration, we note that core confinement was unaffected at the lower density. The pedestal parameters were modified as shown in Fig. 8. In the pedestal region, both edge magnetic shear and q_{95} were systematically increased by 10%-30%. Kinetic profiles were weakly affected by the SF configurations. Pedestal top plasma parameters were modestly changed within $\sim$ 15%: with the SF, T_e^{ped} slightly reduced, n_e^{ped} slightly increased, and p_e^{ped} remained nearly constant. Pedestal energy W_{ped} was nearly unaffected at lower n_e. However, some additional degradation of the pedestal T_e was noted in highly radiative SF configurations, leading to the pedestal energy reduction. Changes in the magnetic shear and weak changes in pedestal pressure gradient did not apparently affect the stability of the peeling-balooning modes, as only small changes in ELM frequency (about 10%-20%) were detected with the SF.

The pedestal stored energy lost per ELM ΔW_{ELM} was reduced, as higher q_{95} increased the pedestal collisionality $\nu^*_{ped} = \pi R q_{95}/\lambda_{e,e}$ and the ELM parallel transit time $\tau_{||}^{ELM} = 2\pi R q_{95}/c_{s,ped}$ (the pedestal ion transport time from the mid plane to the target at the sound speed c_s). This was consistent with the Type I ELM scaling of ΔW_{ELM} with ν^*_{ped} found in many tokamaks [29]. In some discharges, the effect was strong, ΔW_{ELM} was reduced by up to 50% [30], [31]. More typically, however, the reduction was in the range 5%-20%. At higher density in radiative SF divertor discharges, both the ΔW_{ELM} and $\Delta W_{ELM}/W_{ped}$ were lower by 10%-20% (cf. standard divertor) [23].

The SF configuration led to the reduction of ELM energy and ELM peak divertor heat fluxes both at lower n_e and higher n_e (at radiative conditions). In radiative SF divertor experiments in DIII-D both the ΔW_{ELM} and the divertor q_{peak}^{ELM} were reduced more strongly than in standard radiative divertor, leading to the much reduced peak powers. The peak divertor power was reduced in the SF-minus by up to 50-70%, and further reduced in the radiative SF-minus by up to 50%, as compared to the standard divertor [23], suggesting that enhanced radiative dissipation, geometric effects and power spreading all played a role. The analysis of ELM plasma-wetted areas $A_{wet}^{ELM} = P_{div}^{ELM}/q_{peak}^{ELM}$, where P_{div}^{ELM} is the divertor power received during an ELM, showed no systematic trends in the outer divertor, and a reduced A_{wet}^{ELM} in the inner divertor in the SF configuration, both at lower n_e and at higher n_e (radiative) conditions.

V. NSTX Upgrade

The National Spherical Torus Experiment facility has been recently upgraded to new capabilities to enable spherical tokamak physics studies to advance the ST as a candidate for Fusion Nuclear Science Facility [32]. In NSTX-U, discharges with $I_p \leq 2$ MA and $P_{NBI} \leq 12$ MW and up to 5 s duration are projected to produce steady-state peak divertor heat fluxes in excess of 10 MW/m^2. One of the research mission elements of the NSTX Upgrade is the development of advanced plasma-material interface solutions toward future devices [32] The leading heat flux mitigation candidates for NSTX-U are the SF divertor geometry and the impurity-seeded radiative divertor technique, applied to the lower and upper divertors. To enable flexibility in divertor shaping control and SF configurations, an additional divertor coil has been installed in NSTX-U,

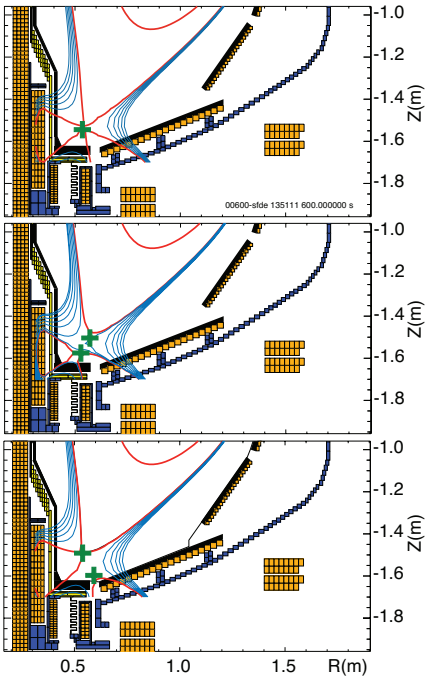

Fig. 10. Modeled SF equilibria for NSTX-U using the initial PF1A, PF1C and PF2L divertor coil set.

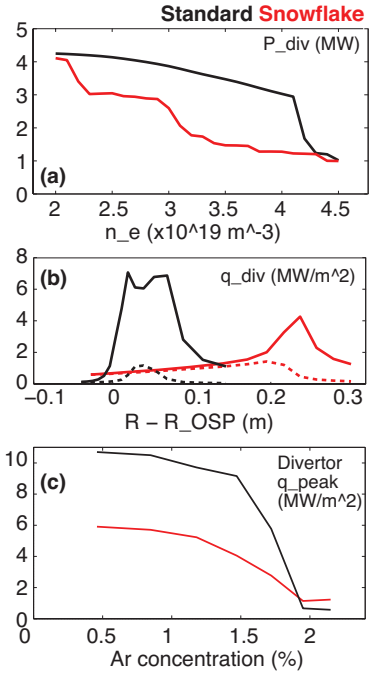

Fig. 11. UEDGE modeling results for NSTX-U standard (black traces) and SF-minus (red traces) divertor configurations. (a) Divertor power as a function of electron density at the core-boundary interface; (b) Divertor heat flux profiles at $n_e = 3.5 \times 10^{-19}$ m^{-3}; (c) Peak divertor heat flux as a function of argon concentration in a radiative Ar-seeded divertor.

as shown in Fig. 10. A number of magnetic equilibria with SF configurations have been modeled successfully using the predictive free-boundary Grad-Shafranov code ISOLVER. The exact SF, SF-minus and SF-plus configurations in the lower an upper divertor regions could be realized with the up-down symmetric set of divertor coils operated below their respective current limits, and with plasma currents up to 2 MA. Four divertor coils should enable control of up to four independent parameters, e.g., positions of the null-points and strike points. Robust SF configurations were obtained in simulations even when time-varying leakage flux from the time-evolving ohmic solenoid current was included [32].

The modeled SF equilibria were also used in predictive edge transport modeling with multi-fluid code UEDGE [33]. Several key NSTX-U results are shown in Fig. 11 [34]. The model used NSTX-like transport coefficients $\chi_{i,e} = 2 - 4$ m^2/s and $D = 0.5$ m^2/s [35], a neutral model using diffusive treatment in cross-field directions and full Navier-Stokes treatment in the parallel direction, a fixed fraction (3 % carbon) impurity and the ion recycling coefficients $R = 1$ at the wall, and $R = 0.99$ at the divertor plates. The power flowing into the SOL was equally split between electrons and ions. The model did not include any special transport modifiers in the null region of the SF configuration, hence, it mostly showed effects of the SF geometry on heat and impurity radiation. The geometric factors were very favorable: in the outer strike point region, $L_{\|} \simeq 20 - 30$ m (c.f. $7 - 15$ m in the standard divertor), and $f_{exp} \leq 40$ (c.f. $10-20$ in the standard divertor). Results for the most challenging $P_{SOL} = 9$ MW, 2 MA case representative of the 12 MW NBI-heated plasma are shown in Fig. 11. A highly radiative scenario occurs in the SF configuration at a much lower density, enabling a greater power loss (w.r.t. the standard divertor), and a larger operating window with reduced q_{div} at lower n_e. Total divertor heat fluxes and the heat fluxes without radiative heating at $n_e = 3.5 \times 10^{-19}$ m^{-3} are shown in Fig. 11 (b). In the outer divertor region, high $q_{peak} \simeq 7$ MW/m^2 was obtained with the standard divertor, and only $3 - 4$ MW/m^2 in the SF-minus configuration. The inner divertor region was found to be highly radiative (possibly with a detached strike point) in both configurations. Impurity-seeded divertors (with neon and argon) were also analyzed. Fig. 11 (c) shows that 50% less argon is needed in the SF-minus configuration to achieve similar q_{peak} reduction factors (cf. standard divertor). The UEDGE modeling results support the SF divertor as a leading steady-state divertor power exhaust solution for NSTX-U.

VI. Discussion and Conclusions

The emerging understanding of inter-ELM and ELM divertor heat transport and radiation in the SF divertor from NSTX and DIII-D experiments provides support to the snowflake divertor configuration as a promising power exhaust concept. In this section we discuss outstanding physics issues that need to be resolved in existing and future tokamaks in order to design a tokamak-based reactor plasma-material interface based on the snowflake divertor concept.

The snowflake configuration has been realized on the NSTX and DIII-D tokamaks without any changes to existing poloidal field coil sets. Equilibria designs were performed using free boundary Grad-Shafranov equilibrium codes. A variety of snowflake divertor equilibria have been modeled for NSTX Upgrade, with both a full coil sets and a reduced coil sets available in initial years. A SF configuration control algorithm

based on the real-time null-tracking [12] is being implemented in the plasma control system.

The SF experiments have shown no detrimental effects on core confinement. The pedestal structure and ELM properties (energy and frequency) have been affected differently in NSTX and DIII-D, suggesting that MHD stability was modified by the presence of the second null. However, the SF effects on the ELM regimes and stability depend on the pedestal stability operating point. A systematic analysis of all possible causes is required, since the effects of higher edge magnetic shear and modified plasma pressure gradient due to the SF could be mixed with the effects of plasma shaping and edge parameter variations. Increased prompt ion loss through the second-order null region was predicted theoretically [36] and may affect the edge electric field and velocity shear, however, no measurements have been performed to verify this.

The increased magnetic flux expansion in the vicinity of the main strike points, the increased connection length in the scrape-off layer, and the increased specific divertor volume have been demonstrated. The geometry modifications led to significantly lower deposited divertor heat fluxes. The exact attribution of this reduction to particular geometry effects was not possible. In both experiments, the strike points generally lied in the SF-induced low B_p zone, hence the flux expansion lowered heat flux in the strike points, sometime to very low levels beyond experimental detection limit. Future SF experiments can focus on divertor heat and particle (impurity) transport studies as functions of geometry properties and plasma collisionality (e.g. in a transition from low-recycling to high recycling and detached), utilizing the SF divertor as a laboratory for divertor physics.

The unique snowflake divertor property of particle and heat flux sharing between additional strike points between and during ELMs was observed experimentally [24]. However, the associated transport mechanism is not well understood and can include particle drifts [37], flute-like and ballooning instabilities that can lead to fast convection [7], [8], [38]–[40], and magnetic field stochastization. Identification and development of a multi-device scaling of the heat flux sharing effect is desirable.

Radiative snowflake experiments used D_2 seeding and intrinsic carbon impurities, or additional impurity seeding (CD_4 in NSTX, neon in DIII-D), and demonstrated additional peak heat flux reduction, including peak ELM heat fluxes ("ELM buffering"), nearly full power detachment, and increased divertor radiation (cf. standard radiative divertor). Again, the results in NSTX and DIII-D differed consistently with the standard radiative divertor differences in the two devices. In NSTX, radiative SF divertor was naturally obtained, and no core confinement degradation was observed. In DIII-D, additional gas seeding was required to induce a radiative SF divertor, and a modest degradation in core confinement was observed. Present studies have not yet addressed radiative SF divertor with high divertor radiated power fractions, e.g., $f_{rad} \geq 0.5 \times P_{SOL}$. The SF impurity radiation distribution, dynamics of radiative condensation instability formation and threshold, impurity screening, and compatibility with particle control techniques (e.g., cryo-pump), and combining the snowflake divertor with applied three dimensional magnetic fields for MHD and ELM control are all outstanding issues and could provide critical information for reactor applications.

In conclusion, recent NSTX and DIII-D experiments have confirmed many predicted snowflake divertor properties, supporting it as an attractive candidate concept for divertor power exhaust in future devices.

ACKNOWLEDGMENTS

This work was performed under the auspices of the US Department of Energy under DE-AC52-07NA27344, DE-AC02-09CH11466, DE-FC02-04ER54698, DE-FG02-07ER54917, and DE-AC04-94AL85000. Both the NSTX and the DIII-D Research Teams are acknowledged for plasma, NBI and diagnostic operations.

REFERENCES

[1] SOUKHANOVSKII, V. A., Advanced divertor magnetic configurations for tokamaks: concepts, status, future. Edge Coorinating Committee Fall Technical Meeting., 2014, http://fire.pppl.gov/APS-DPP14_Divertor_Soukhanovskii.pdf.
[2] RYUTOV, D., Phys. Plasmas **14** (2007) 064502.
[3] PIRAS, F. et al., Phys. Rev. Lett. **105** (2010) 155003.
[4] SOUKHANOVSKII, V. et al., Nucl. Fusion **51** (2011) 012001.
[5] ALLEN, S. et al., Initial snowflake divertor physics studies on DIII-D, in *Proc. 24th IAEA FEC - IAEA CN-197, San Diego, 8-13 October 2012*, Paper PD/1-2, 2012.
[6] CALABRO, G. et al., EAST snowflake experiment: Scenario development and edge simulations, in *Proc. 25th IAEA FEC - IAEA CN-221, St. Petersburg, 16-21 October 2014*, Paper Ex/P3-4, 2014.
[7] RYUTOV, D. D. et al., Plasma Phys. Control. Fusion **54** (2012) 124050.
[8] RYUTOV, D. et al., in *Proc. 24th IAEA FEC, San Diego*, Paper TH/P4-18, 2012.
[9] RYUTOV, D. et al., Phys. Plasmas **15** (2008) 092501.
[10] RYUTOV, D. et al., Plasma Phys. Control. Fusion **52** (2010) 105001.
[11] SOUKHANOVSKII, V. et al., Phys. Plasmas **19** (2012) 082504.
[12] KOLEMEN, E. et al., J. Nucl. Mater., At press (2014).
[13] MANSFIELD, D. et al., J. Nucl. Mater. **390-391** (2009) 764.
[14] MAINGI, R. et al., Phys. Rev. Lett. **103** (2009) 075001.
[15] SOUKHANOVSKII, V. et al., Nucl. Fusion **49** (2009) 095025.
[16] SOUKHANOVSKII, V. et al., Phys. Plasmas **16** (2009) 022501.
[17] SOUKHANOVSKII, V. A. et al., in *Proc. 39th EPS Conf. on Plasma Phys.*, page P5.049, Stockholm, Sweden, 2012.
[18] ROGNLIEN, T. et al., J. Nucl. Mater. **438** (2013) S418.
[19] ITER Physics Expert Group on Divertor et al., Nucl. Fusion **39** (1999) 2391.
[20] LOARTE, A. et al., Nucl. Fusion **47** (2007) S203.
[21] LIPSCHULTZ, B. et al., Nucl. Fusion **47** (2007) 1189.
[22] GREENWALD, M. et al., Nucl. Fusion **28** (1988) 2199.
[23] SOUKHANOVSKII, V. et al., J. Nucl. Mater., At press (2015).
[24] SOUKHANOVSKII, V. A. et al., Developing physics basis for the radiative snowflake divertor at DIII-D, in *Proc. 25th IAEA FEC - IAEA CN-221, St. Petersburg, 16-21 October 2014*, Paper EX/7-4, 2014.
[25] PETRIE, T. et al., Nucl. Fusion **37** (1997) 321.
[26] FENSTERMACHER, M. E. et al., Plasma Phys. Control. Fusion **41** (1999) A345.
[27] PETRIE, T. et al., J. Nucl. Mater. **363–365** (2007) 416.
[28] PETRIE, T. et al., J. Nucl. Mater., At press (2014).
[29] LOARTE, A. et al., J. Nucl. Mater. **313–316** (2003) 962.
[30] HILL, D., Nucl. Fusion **53** (2013) 104001.
[31] YAMADA, H., Nuclear Fusion **53** (2013) 104025.
[32] MENARD, J. et al., Nucl. Fusion **At press** (2012).
[33] ROGNLIEN, T. D. et al., J. Nucl. Mater. **196-198** (1992) 347.
[34] MEIER, E. T. et al., Nucl. Fusion **to be published** (2015).
[35] MEIER, E. et al., J. Nucl. Mater., At press (2015).
[36] RYUTOV, D. et al., Phys. Plasmas **17** (2010) 014501.
[37] CANAL, G. P., *Sawtooth Generated Magnetic Islands and the Properties of the Snowflake Divertor*, PhD thesis, École Polytechnique Federale De Lausanne, 2014.
[38] RYUTOV, D. et al., Contrib. Plasma Phys. **52** (2012) 539.
[39] FARMER, W. et al., Phys. Plasmas **20** (2013) 092117.
[40] RYUTOV, D. et al., Phys. Scripta **89** (2014) 088002.